Assessing a heterogeneous model for accounting for endovascular devices in hemodynamic simulations of cerebral aneurysms

Alain Bérod, Fernando Mut, Juan Cebral, Simon Mendez, Christophe Chnafa, Franck Nicoud

Received: 7 June 2022 | Revised: 18 December 2022 | Accepted: 12 July 2023

DOI: 10.1002/cnm.3762

BASIC RESEARCH

WILEY

Assessing a heterogeneous model for accounting for endovascular devices in hemodynamic simulations of cerebral aneurysms

Alain Bérod[1] | **Fernando Mut**[2] | **Juan Cebral**[2] | **Simon Mendez**[3] | **Christophe Chnafa**[1] | **Franck Nicoud**[3]

[1]Sim&Cure, Montpellier, France

[2]Bioengineering Department, Volgenau School of Engineering, George Mason University, Fairfax, Virginia, USA

[3]CNRS, IMAG, Université de Montpellier, Montpellier, France

Correspondence
Franck Nicoud, Université de Montpellier, CC51, 34095 Montpellier, France.
Email: franck.nicoud@umontpellier.fr

Funding information
GENCI-CINES, Grant/Award Numbers: A0100307194, A0080307194

Abstract

The heterogeneous model developed by Berod et al [*Int J Numer Method Biomed Eng* 38, 2021] for representing the hemodynamic effects of endovascular prostheses is applied to a series of 10 patient specific cerebral aneurysms, 6 being treated by flow diverters, 4 being equipped with WEBs. Two markers correlated with the medical outcome of the treatment are used to assess the potential of the model, namely the saccular mean velocity and the inflow rate at the neck of the aneurysm. The comparison with the corresponding wire-resolved simulations is very favorable in both cases, and the model-based simulations also retrieve the jetting-type flows generated downstream of the struts. Noteworthy, the very same model was used for representing the flow diverters and the WEBs, showing the versatility and robustness of the heterogeneous modeling of the devices.

KEYWORDS

cerebral aneurysms, computational fluid dynamics, endovascular devices, modeling

1 | INTRODUCTION

Over the past decades, minimally invasive treatments of cerebral aneurysms have developed dramatically and are now often preferred to surgical clipping.[1] On top of coils, flow diverters and WEBs are endoprostheses often used by the neuroradiologists,[2,3] the former to handle fusiform aneurysms, the latter to deal with wide neck and saccular ones at bifurcations. In any case, the principle of action of these endovascular treatments is to slow down the flow inside the aneurysm, thus decreasing the dynamic pressure within the sac and associated risk of rupture, and finally stabilizing the aneurysm by promoting thrombosis.

The outcome of a minimally invasive treatment is thus at least partly driven by the hemodynamics inside the aneurysm after implementation of the prosthesis. Although advanced medical imaging techniques like 4D flow magnetic resonance or transcranial Doppler ultrasound can provide relevant information, they suffer from a lack of spatial resolution, only describe the effect of the treatment on the flow a posteriori, and provide limited information about wall shear stress (WSS) and pressure distributions, although new techniques with high fields (7T) are slowly overcoming some of these limitations.[4] Computational fluid dynamics (CFD) does not suffer from the same limitations and has thus

been regarded as a useful complementary modality to analyze the post-treatment hemodynamics. CFD consists in discretizing the Navier–Stokes equations on a spatial mesh to find a relevant solution by using a proper class of algorithm-like finite elements, finite volumes, or lattice Bolzmann. Assuming that the boundary conditions and the rheology of the fluid are known, CFD methods of incompressible flows are now mature and able to provide accurate data in agreement with high-quality measurements.[5,6] Regarding cerebral aneurysms, computational techniques are now commonly used to describe the pretreatment flow under patient-specific conditions[7] for both ruptured and unruptured aneurysms,[8] to characterize the WSS[9] and the development of clot[10] in the sac as well as for supporting the design of a clinically relevant index of the risk of rupture.[11,12]

Two main computational strategies have been used to represent the effects of an endoprosthesis on the hemodynamics inside the aneurysm. The most accurate is the wire-resolved (or conformal) approach where the details of the flow domain, including the network of struts forming the prosthesis, are represented by the computational mesh. This approach was for example used[13] to assess the increase in residence time induced by a flow diverter. Wider databases including 23 aneurysms treated by flow diverters[14] and 36 treated by WEBs[15] have been generated to analyze the relationship between the outcome of the treatment and hemodynamics, showing notably that low volume-averaged saccular velocity and low inflow flow rate at the neck of the aneurysm are potential biomarkers for rapid and complete occlusion. The wire-resolved approach requires that the computational mesh faithfully represent a large range of length scales, typically from a few microns to a few millimeters. This goes with the necessity to handle rather large meshes with 10^7–10^8 elements, thus increasing the computing load dramatically. A way to decrease the CPU time and memory requirements is to model the endovascular device, instead of representing it explicitly. The general idea of porous models[16] is that the set of struts which constitute the prosthesis can be replaced by an artificial interface through which a pressure loss is imposed. The latter is designed to mimic the overall drag generated by each strut when blood flows through the device. Several models have been proposed in the literature[17–20] and applied to realistic configurations. As shown recently,[21] the outcome of an endovascular treatment may strongly depend on the details of the flow interacting with the device as well as on the effective densification of the struts after implementation. Unfortunately, these details cannot be naturally reproduced by the porous method, even if recent efforts to account for the heterogeneity of the porous interface have been made.[18] Moreover, wire-resolved studies show that a jetting-like flow is generated downstream of each mesh of the network of struts; from the clotting perspective, one may anticipate that this kind of flow feature can promote the mechanical activation of the platelets, thus facilitating the occlusion of the aneurysm.

The fact that porous models do not represent flow details potentially relevant to the outcome of the treatment motivated Berod et al[22] to design a heterogeneous immersed model (HIM), with the ambition to gather the accuracy of the wire-resolved simulations and the reduced computational load of the porous models. In this view, source terms located along the centerline of each strut is added to the flow equations to mimic its slowing effect on the flow. Since the dependence on the wire diameter is contained in the source term, there is no necessity to resolve the shape of the struts; the smaller length scale is thus the interwire distance and not the strut diameter as in the wire-resolved simulation, which substantially reduces the computational load. The methodology was successfully applied to a patient-specific aneurysm equipped with a flow diverter[22] but its capability to handle a variety of situations remains to be demonstrated. The objective of this paper is thus to further assess the potential of the heterogeneous model by comparison with a kind of wire-resolved approach, referred to as the embedded model (EM). The cases selected are described in section 2 together with the numerical methods at play. The comparison between modeled-based (HIM) and wire-resolved (EM) simulations is given in section 3 while a discussion relevant to the model limitations and further developments is provided in section 4.

2 | MATERIALS AND METHODS

2.1 | Configurations of interest

We present simulation results for six aneurysms treated with a flow diverter (FD) and four treated with a WEB device. The 10 cases are part of two existing databases[14,15]; to ease the identifications, the IDs from the original publications have been conserved. All the FD-treated cases harbored a side-wall aneurysm in the internal carotid artery (ICA, $n = 6$). WEB-treated aneurysms are located more distally, at arterial bifurcations, in the middle cerebral artery (MCA, $n = 3$) and in the anterior communicating artery (ACOM, $n = 1$). Figure 1 presents the geometry of the 10 cases of interest, together with the geometry and position of the devices. The vessels wall is partially transparent for a better

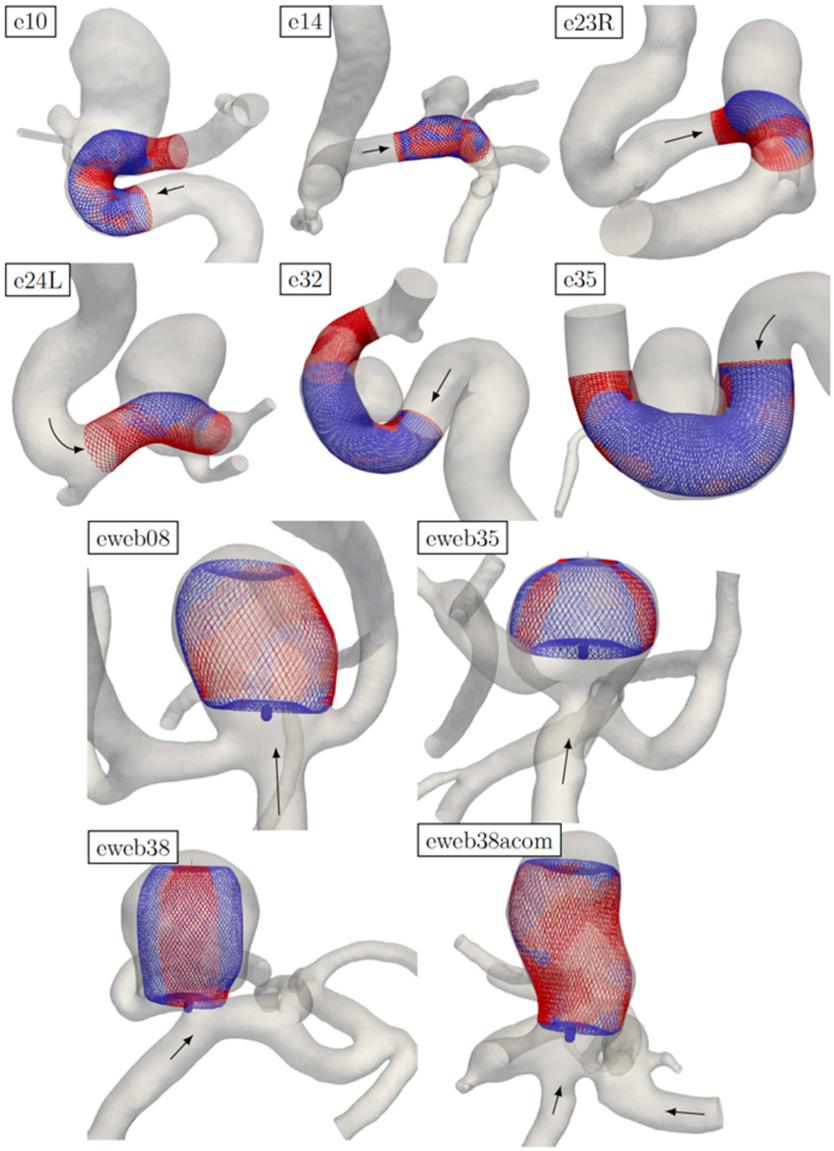

FIGURE 1 Presentation of the computed cases. 3D views of the arterial walls and position of the devices (top: FD and bottom: WEB cases). Configurations are labeled as in the original databases.[14,15] Red wires correspond to parts of the original device (in blue) that were not kept in the HIM computations, since they were either outside or apposed to the wall. For WEB devices, the proximal marker volume, that is, the blue cylinders on the inferior part of the devices, was kept in both embedded model and heterogeneous immersed model computations and modeled as a solid wall. The black arrows indicate the main incoming flows.

visualization of the geometries. The full devices are shown (in blue), with the portions apposed to the wall colored in red. Apposition to the wall was defined with a tolerance of $5D_w$ with D_w the wire diameter ($D_w = 48\,\mu m$ for FDs and $D_w = 25\,\mu m$ for WEBs).

Quantitative characteristics of the cases of interest are presented in Table 1. For each case, the localization, volume, and neck surface of the aneurysm are reported. The number and diameter of the device wires and porosity at the neck are also provided. For each case, delineation of the aneurysm sac from its parent artery was performed manually: it yields an open surface consisting of the aneurysmal wall. This surface was then closed using hole filling tools of the vmtk C++ library[23] and the aneurysmal volume was computed by using this closed surface. Surface delineation and subsequent aneurysm volume computation were performed thanks to vtk C++ libraries.[24] Corresponding neck surface calculation was performed and verified to be close to the reference data.[14,15] Aneurysm volume and neck surface definitions are illustrated in Figure 2A,B.

Virtual deployment of the devices had been performed for the original calculations.[14,15] In short, in silico models of each device were interactively translated and rotated to make the virtual device markers coincide with the actual device

TABLE 1 General characteristics of the cases of interest.

	Aneurysm			Device				
ID	Localization	Sac volume (mL)	Neck surface (mm^2)	Type	Diameter (mm)	Number of wires	Wire thickness (μm)	Neck porosity Mean ± SD [min–max]
e10		0.56	50.6		4			0.6 ± 0.09 [0.22–0.71]
e14		0.03	7.14		3.25			0.64 ± 0.02 [0.53–0.67]
e23R		0.19	33.8		4.75			0.58 ± 0.05 [0.38–0.65]
e24L	ICA	0.28	39.4	FD	4.5	48	48	0.65 ± 0.05 [0.43–0.75]
e32		0.09	23.6					0.42 ± 0.12 [0.065–0.59]
e35		0.13	35.5					0.33 ± 0.14 [0–0.56]
eweb08		0.26	17.7		8			0.57 ± 0.25 [0–0.83]
eweb35	MCA	0.2	21.5	WEB		144	25	0.6 ± 0.25 [0–0.85]
eweb38		0.21	13.1		6			0.45 ± 0.25 [0–0.77]
eweb38acom	ACOM	0.16	9.6		7			0.44 ± 0.25 [0–0.78]

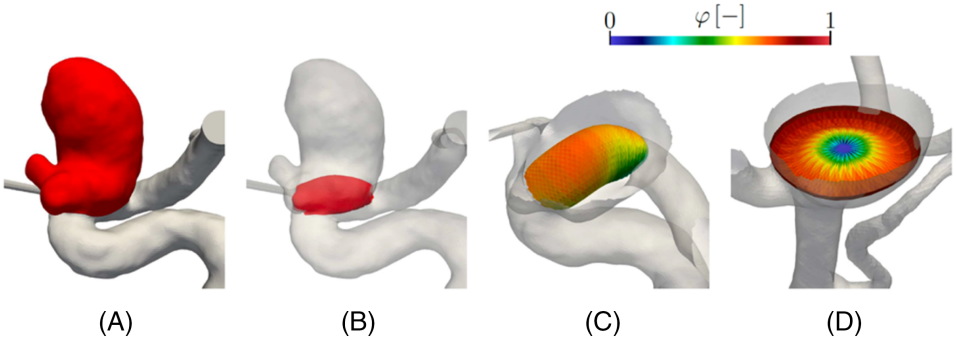

FIGURE 2 Illustration of the definitions of the general characteristics of Table 1: the aneurysm sac (A) and the neck surface (B) are defined manually for each case (here case e10). Illustrations of porosity maps for a FD (case e10, C) and a WEB (case eweb38). The surface is partially clipped for easier visualization.

markers visible in the digital subtraction angiography (DSA) image. The process was repeated with different images acquired in different views to optimize the placement of the 3D virtual device within the vascular model. From the deployed device geometry, porosity maps measuring the local device compaction were calculated. Figure 2C,D presents two examples of porosity maps, whose statistics are gathered in Table 1 for all cases. The porosity φ is defined as the local open area over the local surface area of the device. For FDs, device wires located in inner curvature parts of the parent artery are compacted, with lower device porosity (see Figure 2C). For WEBs, porosity patterns are governed by its design and the grouping of wires at the center of the WEB (see Figure 2D). Overall, mean porosities are similar for both types of devices, but porosity variations at the neck are smaller for FDs than for WEBs.

For each case, blood flow is modeled using incompressible Navier–Stokes equations and a Newtonian fluid rheology, with fixed density of $\rho = 1000\,\mathrm{kg\,m^{-3}}$ and kinematic viscosity $\nu = 4.0\,10^{-6}\,\mathrm{m^2\,s^{-1}}$. At the inlets, the flow rate waveform displayed in Figure 3 is rescaled using the mean flow rate calculated to follow a cube law following the principle of minimum work, as advised by measurements performed by Cebral et al.[25] The shape of the inlet waveform in Figure 3 was obtained from phase-contrast magnetic resonance images for healthy subjects.[26] The pulsatile period was fixed to $T_p = 1\,\mathrm{s}$. A zero-pressure boundary condition is applied at the main outlet. In the case of multiple outlets, the negative flow rate is applied following the profile of Figure 3, with a value of mean flow rate adjusted to obtain typical values of WSS of the order of 1.5 Pa.[25] No-slip wall boundary conditions are applied on the vessel and aneurysm wall, with wall movements neglected. Device modeling is detailed in the next section.

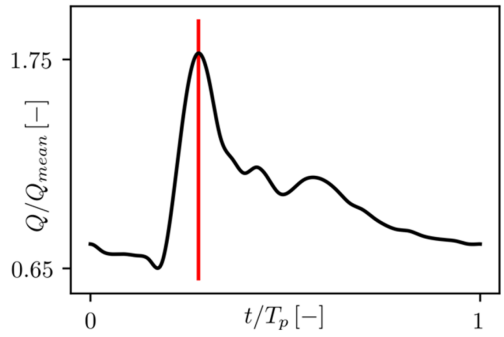

FIGURE 3 Normalized flow rate waveform imposed at the inlet/outlet boundary conditions of the patient-specific cases. The red line corresponds to the peak systole for which comparisons are reported. Q_{mean} is computed with the inlet/outlet diameter cubed such that it produces a typical wall shear stress of 1.5 Pa[25] in the inflow artery.

TABLE 2 Number of cells (in million) for both models EM and HIM and for all the aneurysms considered (post-treatment columns).

	Pretreatment		Post-treatment	
ID	**FEFLO**	**YALES2BIO**	**EM (FEFLO)**	**HIM (YALES2BIO)**
e10	1.6	2.3	52	12.8
e14	0.9	1.3	8.9	6.3
e23R	2.1	3	33	8.9
e24L	2.5	3.6	28	9.7
e32	1.3	2.1	60	13.1
e35	1.7	2.4	107	14.8
eweb08	1.9	2.9	147	11
eweb35	1.8	2.4	150	9.8
eweb38	2.8	3.9	163	21
eweb38acom	1.1	1.7	93	7.7

Note: The meshes used for the pretreatment simulations (no model) performed at George Mason University (FEFLO solver) and Montpellier University (YALES2BIO solver) are also reported (pretreatment columns).
Abbreviations: EM, embedded model; HIM, heterogeneous immersed model.

2.2 | Numerical methods

We compare two different ways of accounting for the effects of the struts of the devices on the flow field. This study takes advantage of existing results obtained with the CFD solver FEFLO from George Mason University authors (J. R. Cebral and F. Mut), using a wire-resolved type of approach, namely the embedded modeling (EM) of devices[27] (see section 2.2.1). Then, a second CFD solver called YALES2BIO and developed at the University of Montpellier was used to predict the same cases with a heterogeneous immersed method[22] (HIM); whenever relevant, results from an homogeneous porous method[17] (PM) implemented in the same flow solver as HIM were also included for comparison (see section 2.2.2). Of course, the pretreatment cases were computed by using the two flow solvers independently to make sure that the numerical results before the device implementation were in good agreement—see Table 2.

2.2.1 | Numerical methods for the wire-resolved (EM) calculations

The first CFD solver used in this study is an in-house edge-based finite element solver for the unsteady incompressible Navier–Stokes equations (FEFLO) developed at George Mason University. The solver is fully implicit, and the incompressibility condition is attained using a projection scheme that results in the resolution of a pressure Poisson[7] equation. The modeling of the wire struts starts with the initial water-tight mesh defining the vascular model

(aneurysm + adjacent vessels) and performing several mesh refinements sweeps over the mesh until the local element size reaches about 1/8 of the wire strut diameter which has been determined to be sufficient for realistic flow field representations.[27] This mesh is then loaded into the field solver and all the edges that intersect the wire struts are identified and no-slip boundary conditions are applied at the intersection points.[7] For more details, see References 28,29.

2.2.2 | Numerical methods for the prosthesis modeled (HIM or PM) calculations

The second CFD solver used in this study is the in-house finite-volume YALES2BIO (https://imag.umontpellier.fr/~yales2bio/index.html). YALES2BIO is a massively parallel finite-volume solver dedicated to blood flow computations, which has been used and validated in many configurations.[5,6,30–35] YALES2BIO solves the Navier–Stokes equation with minimally dissipative fourth-order spatial and time discretization schemes to explicitly advance the velocity field. A pressure-projection method is used to handle the incompressibility constraint, which leads to solving a Poisson equation for the pressure using a Deflated Preconditioned Conjugated Gradient solver.[36]

Heterogeneous immersed modeling of the struts

The heterogenous model from Bérod et al[22] is one of the three methods used in this study to represent the struts. The principle is to apply, at the level of the struts, a source term designed to mimic the effect of the struts on the flow on the three components of the velocity, locally rotated in the frame of the device. The source terms are designed with the following assumptions: the device is assumed to be well represented locally as a combination of two families of parallel struts of local interwire distance and interfamily angle. Effects of neighboring walls are neglected and the source term from each family of struts is applied independently of the other, that is, there is no specific model for the wire crossings. Finally, curvature effects were neglected. The model consists in correlating the force applied by a family of parallel struts on the flow with the incident velocity. If the interwire distance is large, the force tends to the one obtained for a unique cylinder. The structure of the algorithm is the following:

1. The device is first triangulated to obtain a surface mesh independent of the fluid volumetric grid. For each triangle, the local flow rate is computed by interpolating the fluid velocity field. From the local flow rate and the local characteristics of the device, a correlation established from a numerical database allows the estimation of the incident velocity,[22]
2. For each wire segment, the incident velocity is rotated into the local frame of the device, to obtain a normal component, a longitudinal component along the wire direction and a tangential component forming an orthonormal basis. Then, correlations are used to calculate the forces in the three directions,[22] depending on the incident velocity and wire characteristics. The expression of the forces can be found in the Appendix and Figure A1. See the methodology article[22] for more details about the model and its justification,
3. Then, the force known for each wire segment is regularized on the fluid grid thanks to an adapted version of the Reproducing Kernel Particle Method.[12,22,37] Navier–Stokes equations are then solved with the forcing coming from the device struts. The forcing is updated at each iteration of the fluid solver.

Note that this method needs to have sufficient refinement in the region of the device. In practice, the mesh size is fixed to $\Delta x = W/8$, with W the typical interwire distance. Recall that the mesh size is only 1/8 of the strut diameter for the EM approach (see section 2.2.1); it follows that the number of elements required by the HIM approach is significantly smaller (up to 15 times for the eweb35) than what is required for EM—see Table 2. Using $\Delta x = W/8$ for the mesh size proved sufficient to properly describe the jets that form between the wires. Validation of the method has been performed in Berod et al[22] by comparison with a database of fully resolved simulations of various complexity.

Porous modeling of the device

To ease comparison, the porous model from Raschi et al[17] has also been implemented in the YALES2BIO solver. The surface of the device is modeled as a porous layer with a localized pressure loss when the fluid passes through. A systematic thickness of $\Delta L = 0.2$ mm was given to the layer, to define a volume over which a volumetric source term $\boldsymbol{f}$ is added to the Navier–Stokes equations. The mesh was specifically refined to ensure that four grid cells span the layer thickness. The model[17] reads:

$$\boldsymbol{f} = -(D\boldsymbol{u} + F||\boldsymbol{u}||\boldsymbol{u}), \text{with } D = 0.75\frac{11\rho\nu}{d_h\Delta L} \text{ and } F = 0.86\frac{\rho}{2\Delta L}\left(1.3(1-\varphi) + \left(\frac{1}{\varphi} - 1\right)^2\right).$$

The mathematical expressions of D and F come from experimental correlations[38] and the leading coefficients are corrections related to the application of the source term on an unstructured grid, with an involved volume slightly larger than ΔL.[17] This porous model uses the correlations established for the pressure drop in the case of a flow normal to a screen of given porosity and applies it as a source term on each velocity component. It has been proven to produce relatively good results in Raschi et al.[17] It is used here as an example of porous model, but alternatives exist.[16,18–20]

2.3 | Postprocessing of the results

Results with and without device and for the different simulation strategies will be qualitatively analyzed using velocity maps at peak systole (see Figure 3). Quantitative comparisons will be presented using relevant quantities for the assessment of treatment by FDs[14,39] or WEBs.[15] The first one is the magnitude of the space and time-averaged intrasaccular velocity defined as:

$$U_a = \frac{1}{V_a}\int_{\Omega_a} \left\| < U > \right\| dv$$

with Ω_a the aneurysm domain and V_a the corresponding volume, reported in Table 1. $< U >$ is the time-averaged velocity vector while $\|\cdot\|$ denotes the Euclidian norm.

The second quantity used for comparison is the peak-systolic inflow rate at the neck:

$$Q_p = \int_{\Gamma_n^p} U.nds,$$

with Γ_n^p the portion of the aneurysm neck surface where $U.n > 0$, n the normal vector to the neck surface pointing toward the aneurysm and U the velocity vector. Q_p measures the blood exchanges between the parent artery and the aneurysm sac.

For U_a and Q_p, both absolute values and decrease in the indices due to treatment will be compared between the different computational strategies for stenting.

3 | RESULTS

Results from the heterogeneous model of Bérod et al[22] are compared to wire-resolved simulations of a variety of cerebral aneurysms treated by either flow diverter[14] or intrasaccular WEBs[15]; results from the porous model[17] are also introduced when appropriate.

3.1 | Qualitative comparison

Typical results for flow diverters and WEBs are shown in Figures 4 and 5, respectively. In both cases, a 3D view of the region of interest is included (see panel [A]) to appreciate the geometric complexity and to localize the slices used for visualizing the velocity maps. The pretreatment situations are shown in the (B) panels, revealing the jetting flow that crosses the neck of the aneurysms. This flow structure maintains the blood motion inside the sacs, which prevents thrombosis and stabilization of the aneurysm. Its impingement on the dome (see white circles) may weaken the aneurysmal tissue and favor either its expansion and/or rupture due to the extra dynamic pressure. To the first order, the objective of any endo-vascular treatment is to weaken this incoming flow, thus decreasing the intrasaccular velocity and increasing the time of residence to favor thrombosis.

Figures 4C and 5C show the meshes used for performing the wire-resolved simulations[14,15] of the post-treatment cases while Figures 4D and 5D display the corresponding maps of velocity magnitude. The impact of the devices is clearly visible, the jetting flow being drastically reduced in both cases. Note the mesh refinement in the region of the devices, the size of the element being small enough to allow a fair geometric representation of the struts diameter (the total number of elements of the meshes is 28 M [Figure 4] and 147 M [Figure 5]). When using the heterogeneous model,[22] the mesh is only required to represent the interwire distance, which is typically 5–10 times larger than the strut diameter. As a direct consequence, the total number of elements required for the heterogeneous model-based simulations is significantly smaller than for the brute force approach, of the order of 10 M for the two cases displayed. Note however that the resolution in the aneurysmal sac is slightly better in the model-based simulations (cf. Figure 4C,E on the first hand, and Figure 5C,E on the other hand) to ensure the best quality of the outcome.

Comparing Figures 4D,F and 5D,F shows that the model-based approach reproduces nicely the modification induced by the flow diverter and the WEB. The secondary flow structures induced by the WEB and visible on both sides of the stopped jet, below the WEB boundary (see the white circles in Figure 5D) are also very well retrieved by the model-based computation, as indicated in Figure 5F. The same figure also shows that the small wakes and jets generated by the wire meshes of the WEB structure (see the white*) in the wire-resolved (EM) simulations are also retrieved by the heterogeneous model, even if the wires are not explicitly resolved; note however that the orientations of these small flow features are somewhat different from their counterparts in the wire-resolved computation (see Figure 5D). Such wakes and jets structures also exist in the flow diverter configuration displayed in Figure 4, but their typical size is smaller. Still, the wires collectively generate a region of low velocity in the sac whose shape and intensity obtained by the model-based approach are in well agreement with the wire-resolved (EM) solutions. A more quantitative assessment of the performances of the method is proposed in the following section.

3.2 | Global quantities

Quantitative comparisons for the whole set of simulations (six flow diverters and four WEBs) are displayed in Figure 6 (volume-averaged velocity magnitude) and Figure 7 (inflow rate at the neck). These two macroscopic quantities were selected for their positive correlation with the outcome of the treatment of aneurysms by endovascular devices[39,40] and potential use in the clinical environment, as both of them could be assessed retrospectively from advanced medical imaging techniques like 4D flow MRI. These integral quantities are robust to any noise in the measurements, contrarily

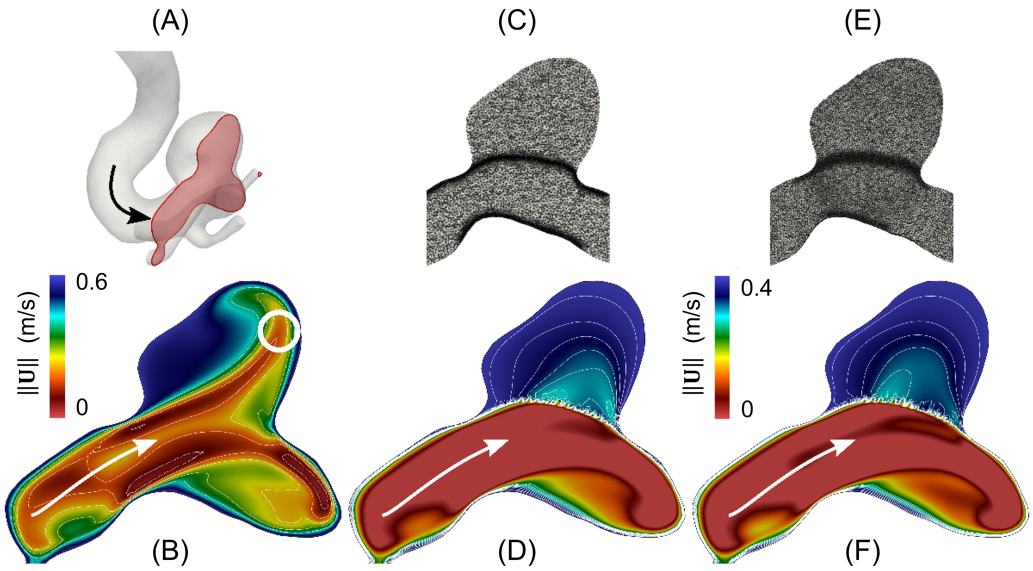

FIGURE 4 Peak-systolic velocity magnitude for case e24L. (A): slice location in the 3D geometry of the aneurysm. (B): pretreatment velocity field in the slice displayed in (A); the white arrows show the main direction of the upstream flow and the white circle indicates the region where the jetting flow impacts the dome. Post-treatment mesh and velocity map projected onto the slice for the wire-resolved simulation (C, D) and the heterogeneous[22] (E, F) model.

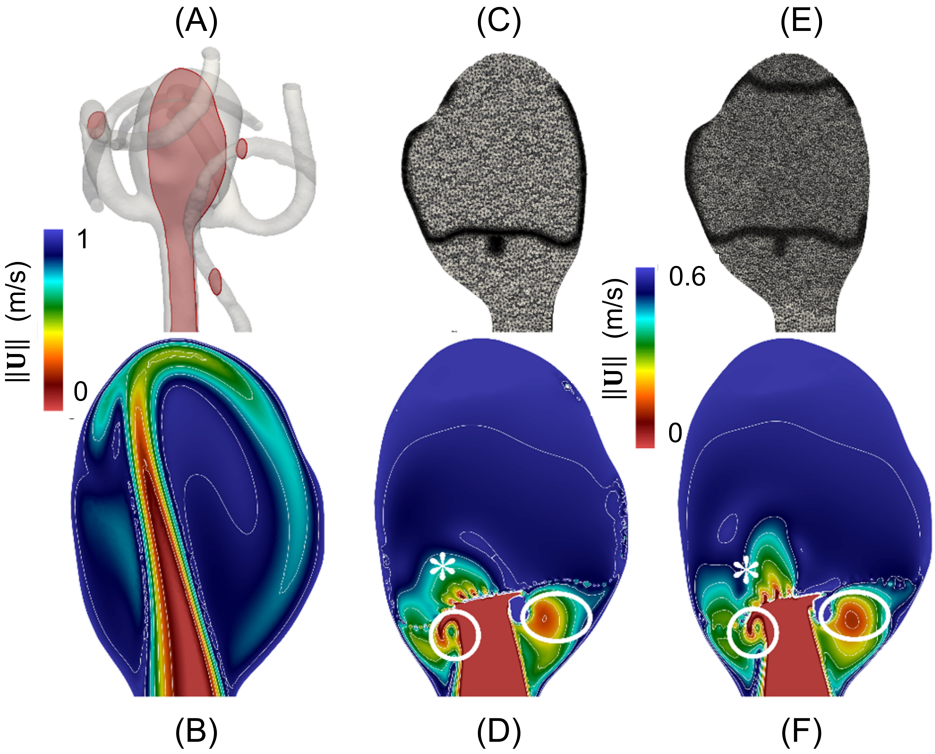

FIGURE 5 Case eweb08; see Figure 4 for the description.

to local quantities (e.g., map of WSS) which may strongly depend on uncertain data such as the geometry and its changes over the cardiac cycle. From Figures 6A,B and 7A,B, the pretreatment values obtained with the two flow solvers (see section 2) are generally in very close agreement, even if obtained using different numerical strategies and meshes. The largest discrepancy is for the case e14 and corresponds to approximately 10%, far less than the effect of the endovascular treatment on the averaged velocity.

The post-treatment reduction of the aneurysmal velocity is presented in Figure 6C,D while the results relevant to the inflow rate at the neck are displayed in Figure 7C,D. The porous model of Raschi et al[17] performs reasonably well in most of the cases (36% and 40% average error for the aneurysmal velocity and inflow rate, respectively). Note that the porous model, which relies on the concept of averaged porosity over the neck, is only applied to flow diverters given the large heterogeneous porosity of WEBs. The main issue with the porous model is twofold: (1) a pronounced trend to overestimate the inflow rate, and to a lesser extent the mean velocity; (2) the possibility to generate large errors in some specific cases, for example 100% error in the reduction of the aneurysmal velocity for case e32. This lack of robustness may question the use of the model as a predictive tool to study configurations for which the ground truth is not known.

The heterogeneous model[22] reproduces all the trends observed in the wire-resolved simulations,[14,15] for all the flow diverter and WEB cases considered. The model performances are even more noteworthy that the range of reduction of both macroscopic quantities is rather large, from approximately 10% (case e35) to 60% (case eweb35) for the averaged velocity (see Figure 6C,D) and from 15% (case eweb38acom) to 65% (case eweb35) for the inflow rate entering the sac (see Figure 7C,D). The average error in reduction is approximately 6% for the flow diverters, and 8% for the WEBs (scanning both macroscopic quantities) while it is 4% for the averaged velocity and 10% for the inflow rate reduction (scanning both device types). Note also that the maximum error is only 8% for the averaged velocity (case eweb38) and 20% for the inflow rate (case eweb38acom). These results mean that the heterogeneous approach[22] is not only efficient but also robust, a desirable property for any model.

3.3 | Further analysis

It appears from Figures 6 and 7 that the velocity and inflow rate reductions differ depending on the case considered. For example, the velocity reduction is about 35% for the case e24L, but only 15% for e32, both treated with a flow

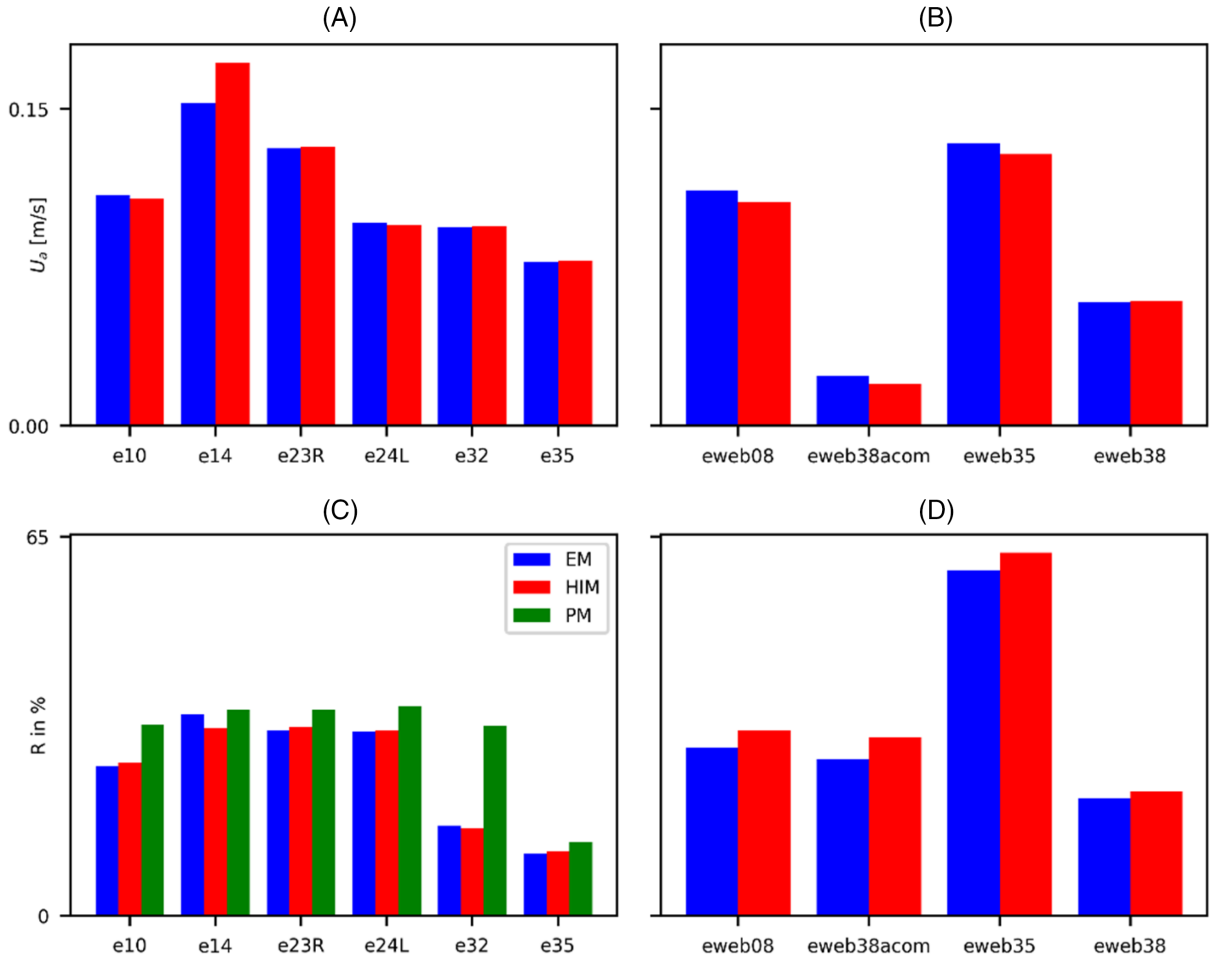

FIGURE 6 Volume averaged velocity magnitude in the aneurysm. Pretreatment values from the present study and the published data for flow diverters[14] (A) and WEBs[15] (B). Post-treatment velocity reduction from the wire-resolved simulations[14] (EM—blue), the heterogeneous model[22] (HIM—red), and a porous model[17] (PM—green) for the flow diverters cases (C), from the resolved simulations[15] (EM—blue) and the heterogeneous model[22] (HIM—red) for the WEB cases (D). EM, embedded model; HIM, heterogeneous immersed model.

diverter. To illustrate the versatility of the heterogeneous model, the reasons why the device performance is reduced in the e32 case are exposed in what follows. First, e32 is located on the inner-curvature part of the arterial wall, as shown in Figure 8. Therefore, contrary to other typical cases (see Figure 1), the incoming flow does point toward the aneurysm dome. Moreover, large mal-apposed portions of the device remain upstream of the aneurysm (see Figure 8). It results that the tangential drag force component is more important than the normal one, challenging any device model even more than usual.

Still, the heterogeneous model[22] succeeds in reproducing the post-treatment flow structure, as shown in Figure 9. Not only the averaged mean saccular velocity is well retrieved (see Figure 6), but the agreement on the remaining intrasaccular jet characteristics between wire-resolved and heterogeneous model-based simulations is good, as shown by the velocity vectors displayed in Figure 9C–E. At the same time, and consistently with the poor performance already observed for the porous model (see Figure 6), the homogeneous formulation does not give a proper assessment of the flow structure, neither inside nor outside the sac. Two main reasons may be put forward to this regard. On the one hand, porous models are mostly designed to reproduce pressure load along the normal direction of the device, while tangential effects are prominent here. On the other hand, some wires located in the inner part of the parent artery are densely packed due to device compression, which produces non-uniform porosity patterns throughout the device surface (not shown), while the porous model was tuned by assuming uniform porosity.[17] These two features make the porous formulation fail but can be nicely handled by the heterogeneous model, as illustrated in Figure 9.

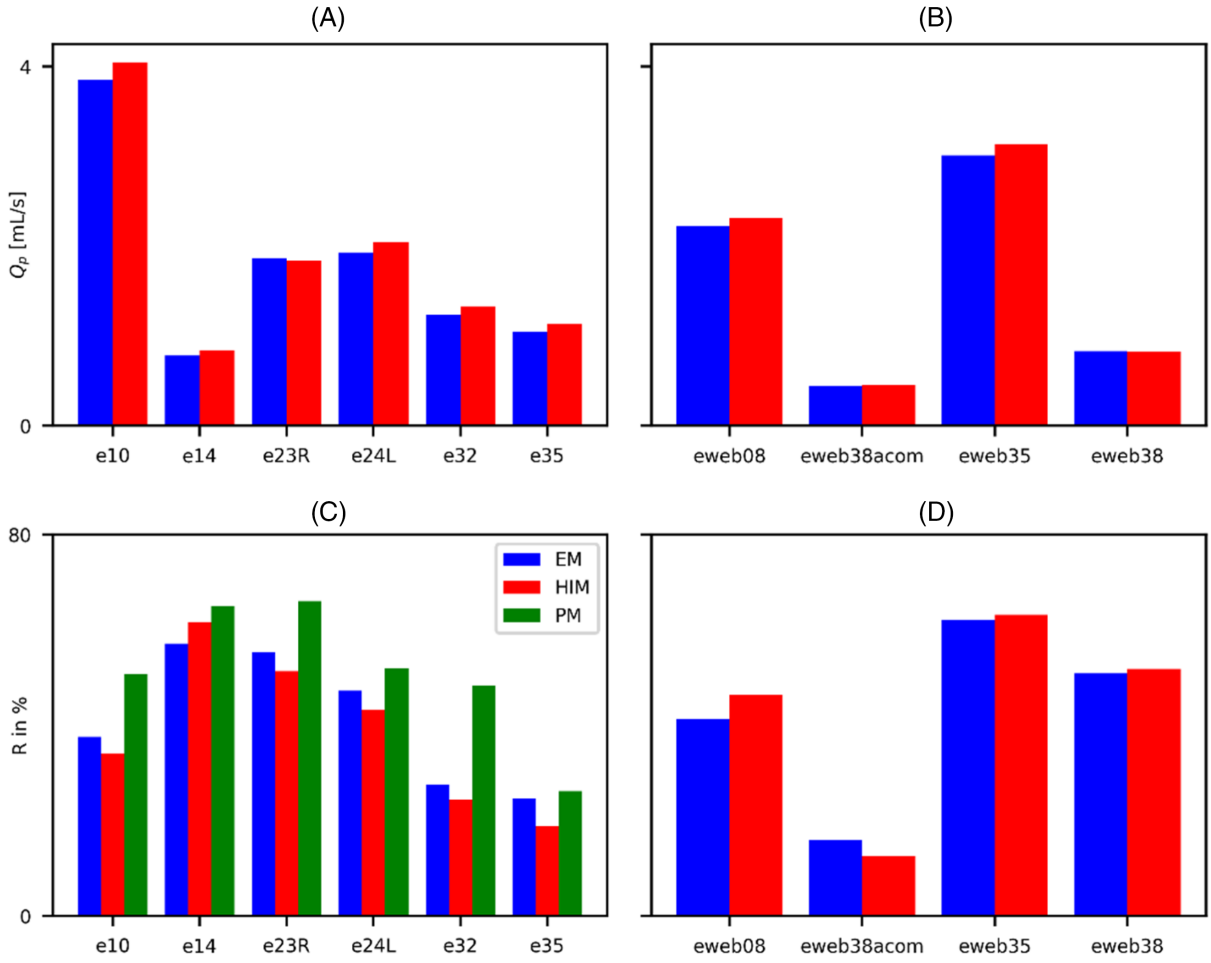

FIGURE 7 Inflow rate at the aneurysm neck. See Figure 6 for the description.

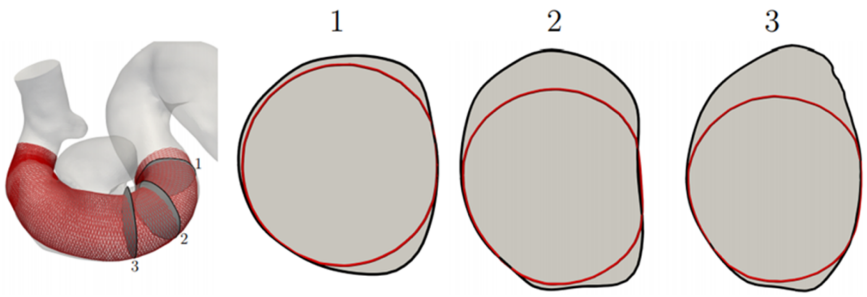

FIGURE 8 Mal-apposition of the flow diverter e32 case.

4 | DISCUSSION

The heterogeneous model developed in Berod et al[22] is shown to quantitatively reproduce wire-resolved results from the GMU group.[14,15] Most notably, jetting-flows between struts as well as intrasaccular velocity reductions and redirections are captured, for both FD and WEB cases. Moreover, the model has demonstrated its versatility, compared to porous models, to account for both mal-apposed device portions and distinctive characteristics such as inward parent artery curvature. Although initially developed and validated for a single typical FD-treated aneurysm,[22] the heterogeneous model applicability was further extended to other type of braided device, namely intrasaccular WEBs, without any model modification other than the implementation of a penalization driving the blood velocity to zero for extremely dense wires found at the recess. This confirms again the versatility of the heterogeneous modeling approach.

Despite the success shown in this paper, a few limitations regarding the heterogeneous technology as well as the present validation effort must be mentioned. Contrary to simpler porous models where the struts are not kept, the mesh resolution must be fine enough to represent faithfully the jets induced by the networks of struts. From our experience, the grid spacing should not be larger than one eighth of the interwire distance, thus typically 100 μm in the neck region. This also means that the number of cells is dependent on the device characteristics, the denser the networks of struts, the finer the computational mesh. This undesirable link is the price to pay for being able to reproduce the jetting-like flows generated by the device as well as heterogeneities in the porosity patterns throughout the device surface. Note also that the heterogeneous modeling approach requires some coding and data management before it can be used in a standard flow solver to perform the force computation and regularization (see section 2.2.2). These operations induce an extra computational cost of approximately 12% for a typical endovascular device.[22] Despite this, the gain with respect to the wire-resolved approach, where the minimal length scale is imposed by the strut diameter rather than the inter-wire distance, is considerable. This was precisely measured in Reference 22 for a typical flow diverter for which the memory usage was reduced by a 22 factor, while the computational cost was divided by 5766. The latter reduction is partly explained by the time-step reduction (factor 300) induced by the mesh coarsening in the explicit solver used in Reference 22. A more conservative reduction factor of $5766/300 \sim 20$ can be inferred for a flow solver with implicit time-stepping.

Another limitation is the modeling of the forces induced by each wire and which relies on two main assumptions[22]: the curvature of the device can be neglected and the flow regime is inertial. Both assumptions are valid in most of the cases, thus the successful comparison obtained in this study. Still, some extra errors may appear when either assumption is not met. A closer inspection of the case eweb38, for which the error in the mean velocity is the largest, shows that after deployment the curvature of the struts can be very large locally, of the order 10^3 m^{-1}. It turns out that the model performed well even for this extreme case, but one cannot exclude that this is by chance. Further developments of the wire-induced force should include the curvature effect. The same is true for the flow regime, which is assumed inertial at the scale of the strut diameter in Berod et al.[22] However, with the current trend to use smaller and smaller strut size to minimize the amount of artificial material brought by the treatment and the presence of low blood flow velocity near arterial wall, the flow regime is most probably diffusive for at least some of the wires. A mixture of inertial/diffusive force expressions would be useful to make the heterogeneous model even more versatile.

It has been decided not to compare WSS values between the simulations. Such a comparison would be interesting, but no specific work has been undertaken to converge the values of WSS (with near-wall refinement to reach grid

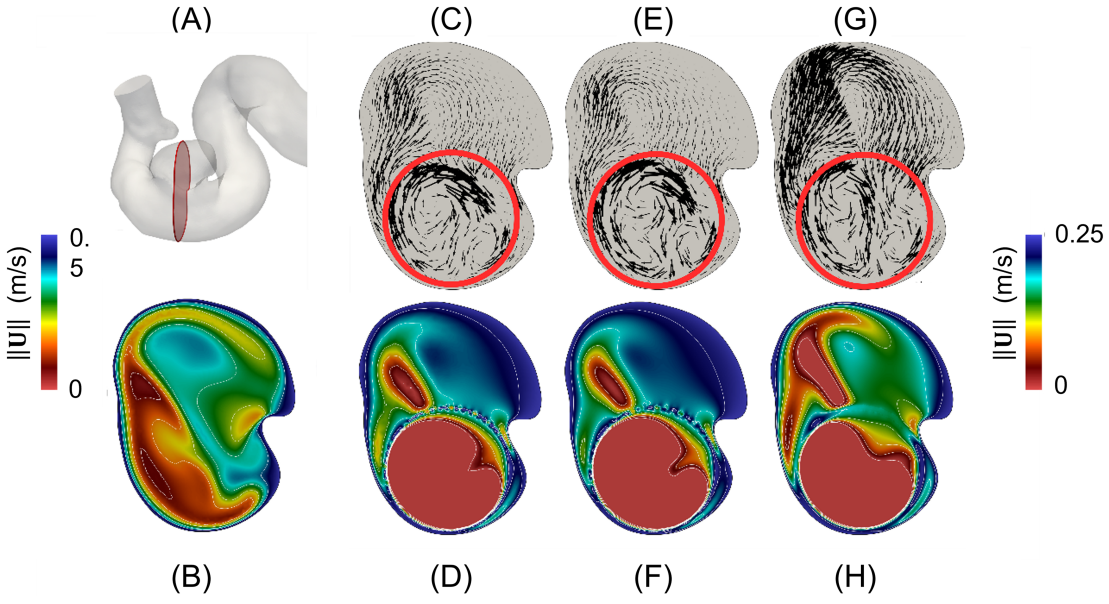

FIGURE 9 Velocity magnitude for case e32. (A): slice location in the 3D geometry of the aneurysm. (B): pretreatment velocity field in the slice displayed in (A). Post-treatment velocity vectors projected onto the slice and map of velocity magnitude for the wire-resolved simulation (C, D), the heterogeneous[22] model (E, F) and the porous model[17] (G, H). The red line in (C, E, G) denotes the position of the flow diverter.

convergence). In this context, WSS maps are not expected to assess the relevance of the modeling of the devices, but rather the mesh quality at the wall, which is not the focus of the study. Still, the U_a quantity provides an indication about the reduction in WSS provided by the treatment.

Comparing different flow solutions in complex geometries is a complex task. In the present study, two global quantities particularly relevant to the outcome of the endovascular treatment were used, namely the volume averaged velocity magnitude in the aneurysm and the inflow rate at the neck. As any global quantity, they have the advantage to be robust to the details of the geometry and numerical procedures. Still, they may also hide some measurable differences which could be induced by the model. For example, computing the norm of the pointwise difference between the wire-resolved and wire-modeled velocity fields would give a more detailed view of the discrepancies. Still, this procedure can produce large errors even if the two computational modalities lead to flows having very similar structures, namely some jetting-flows downstream of the device and mostly zero velocity in the core of the aneurysmal sac. To exemplify this statement, the volume-averaged pointwise error scaled by the U_a quantity is almost 25% for the case eweb08 displayed in Figure 5, while the error based on U_a is merely 5%. Defining a fair measure of the resemblance between two solutions would be useful during further model improvements.

ACKNOWLEDGMENTS

Simulations with YALES2BIO were performed using HPC resources from GENCI-CINES (Grant Nos. A0080307194 and A0100307194) and with the support of the MESO@LR-Platform at the University of Montpellier.

CONFLICT OF INTEREST STATEMENT

The authors declare no conflict of interest.

DATA AVAILABILITY STATEMENT

The data that support the findings of this study are available from the corresponding author upon reasonable request.

ORCID

Alain Bérod https://orcid.org/0000-0001-8433-5788
Fernando Mut https://orcid.org/0000-0003-1907-3739
Juan Cebral https://orcid.org/0000-0002-3216-0856
Franck Nicoud https://orcid.org/0000-0002-0006-8422

REFERENCES

1. Lee KS, Zhang JJY, Nguyen V, et al. The evolution of intracranial aneurysm treatment techniques and future directions. *Neurosurg Rev*. 2022;45:1-25.
2. Rajah G, Narayanan S, Rangel-Castilla L. Update on flow diverters for the endovascular management of cerebral aneurysms. *Neurosurg Focus*. 2017;42(6):E2.
3. Dmytriw AA, Salem MM, Yang VXD, et al. Endosaccular flow disruption: a new frontier in endovascular aneurysm management. *Neurosurgery*. 2020;86:170-181.
4. Gottwald LM, Töger J, Markenroth Bloch K, et al. High spatiotemporal resolution 4D flow MRI of intracranial aneurysms at 7T in 10 minutes. *Am J Neuroradiol*. 2020;41:1201-1208.
5. Puiseux T, Sewonu A, Meyrignac O, et al. Reconciling PC-MRI and CFD: an in-vitro study. *NMR Biomed*. 2019;32:e4063.
6. Zmijanovic V, Mendez S, Moureau V, Nicoud F. About the numerical robustness of biomedical benchmark cases: interlaboratory FDA's idealized medical device. *Int J Numer Method Biomed Eng*. 2017;33:1-17.
7. Cebral JR, Castro MA, Appanaboyina S, Putman CM, Millan D, Frangi AF. Efficient pipeline for image-based patient-specific analysis of cerebral aneurysm hemodynamics: technique and sensitivity. *IEEE Trans Med Imaging*. 2005;24:457-467.
8. Cebral JR, Mut F, Weir J, Putman C. Quantitative characterization of the hemodynamic environment in ruptured and unruptured brain aneurysms. *Am J Neuroradiol*. 2011;32:145-151.
9. Evju Ø, Valen-Sendstad K, Mardal KA. A study of wall shear stress in 12 aneurysms with respect to different viscosity models and flow conditions. *J Biomech*. 2013;46:2802-2808.
10. Ngoepe MN, Ventikos Y. Computational modelling of clot development in patient-specific cerebral aneurysm cases. *J Thromb Haemost*. 2016;14:262-272.
11. Sanchez M, Ambard D, Costalat V, Mendez S, Jourdan F, Nicoud F. Biomechanical assessment of the individual risk of rupture of cerebral aneurysms: a proof of concept. *Ann Biomed Eng*. 2013;41:28-40.
12. Sanchez M, Ecker O, Ambard D, et al. Intracranial aneurismal pulsatility as a new individual criterion for rupture risk evaluation: biomechanical and numerical approach (IRRAs project). *Am J Neuroradiol*. 2014;35:1765-1771.

13. Janiga G, Rössl C, Skalej M, Thévenin D. Realistic virtual intracranial stenting and computational fluid dynamics for treatment analysis. *J Biomech*. 2013;46:7-12.
14. Mut F, Raschi M, Scrivano E, et al. Association between hemodynamic conditions and occlusion times after flow diversion in cerebral aneurysms. *J Neurointerv Surg*. 2015;7:286-290.
15. Cebral JR, Chung BJ, Mut F, et al. Analysis of flow dynamics and outcomes of cerebral aneurysms treated with intrasaccular flow-diverting devices. *Am J Neuroradiol*. 2019;40:1511-1516.
16. Augsburger L, Reymond P, Rufenacht DA, Stergiopulos N. Intracranial stents being modeled as a porous medium: Flow simulation in stented cerebral aneurysms. *Ann Biomed Eng*. 2011;39:850-863.
17. Raschi M, Mut F, Löhner R, Cebral J. Strategy for modeling flow diverters in cerebral aneurysms as a porous medium. *Int J Numer Method Biomed Eng*. 2014;30:909-925.
18. Dazeo N, Dottori J, Boroni G, Narata AP, Larrabide I. Stenting as porous media in anatomically accurate geometries. A comparison of models and spatial heterogeneity. *J Biomech*. 2020;110:109945.
19. Yadollahi-Farsani H, Scougal E, Herrmann M, et al. Numerical study of hemodynamics in brain aneurysms treated with flow diverter stents using porous medium theory. *Comput Methods Biomech Biomed Eng Imaging*. 2019;22:961-971. 10.1080/10255842.2019.1609457
20. Li S, Chopard B, Latt J. Continuum model for flow diverting stents in 3D patient-specific simulation of intracranial aneurysms. *J Comput Sci*. 2019;38:101045.
21. Chodzyński KJ, Uzureau P, Nuyens V, Rousseau A, Coussement G, Zouaoui Boudjeltia K. The impact of arterial flow complexity on flow diverter outcomes in aneurysms. *Sci Rep*. 2020;10:10337.
22. Berod A, Chnafa C, Mendez S, Nicoud F. A heterogeneous model of endovascular devices for the treatment of intracranial aneurysms. *Int J Numer Method Biomed Eng*. 2021;38:e3552.
23. Antiga L, Piccinelli M, Botti L, Ene-Iordache B, Remuzzi A, Steinman DA. An image-based modeling framework for patient-specific computational hemodynamics. *Med Biol Eng Comput*. 2008;46:1097-1112.
24. Schroeder W, Martin K, Lorensen B. *The Visualization Toolkit: an Object-Oriented Approach to 3D Graphics*. 3rd ed. Kitware; 2018 http://www.kitware.com/products/vtktextbook.html
25. Cebral JR, Castro MA, Putman CM, Alperin N. Flow-area relationship in internal carotid and vertebral arteries. *Physiol Meas*. 2008;29:585-594.
26. Ford MD, Alperin N, Lee SH, Holdsworth DW, Steinman DA. Characterization of volumetric flow rate waveforms in the normal internal carotid and vertebral arteries. *Physiol Meas*. 2005;26:477-488.
27. Appanaboyina S, Mut F, Löhner R, Putman CM, Cebral JR. Computational fluid dynamics of stented intracranial aneurysms using adaptive embedded unstructured grids. *Int J Numer Methods Fluids*. 2008;57:475-493.
28. Appanaboyina S, Mut F, Löhner R, Putman C, Cebral J. Simulation of intracranial aneurysm stenting: techniques and challenges. *Comput Methods Appl Mech Eng*. 2009;198:3567-3582.
29. Mut F, Chung BJ, Chudyk J, et al. Image-based modeling of blood flow in cerebral aneurysms treated with intrasaccular flow diverting devices. *Int J Numer Method Biomed Eng*. 2019;35:e3202. doi:10.1002/cnm.3202
30. Lanotte L, Mauer J, Mendez S, et al. Red cells' dynamic morphologies govern blood shear thinning under microcirculatory flow conditions. *Proc Natl Acad Sci*. 2016;113:13289-13294.
31. Méndez Rojano R, Mendez S, Nicoud F. Introducing the pro-coagulant contact system in the numerical assessment of device-related thrombosis. *Biomech Model Mechanobiol*. 2018;17:815-826.
32. Iss C, Midou D, Moreau A, et al. Self-organization of red blood cell suspensions under confined 2D flows. *Soft Matter*. 2019;15:2971-2980.
33. Taraconat P, Gineys J-P, Isèbe D, Nicoud F, Mendez S. Numerical simulation of deformable particles in a coulter counter. *Int J Numer Method Biomed Eng*. 2019;35(11):e3243. doi:10.1002/cnm.3243
34. Puiseux T, Sewonu A, Moreno R, Mendez S, Nicoud F. Numerical simulation of time-resolved 3D phase-contrast magnetic resonance imaging. *PloS One*. 2021;16:e0248816.
35. Chnafa C, Mendez S, Nicoud F. Image-based simulations show important flow fluctuations in a normal left ventricle: what could be the implications? *Ann Biomed Eng*. 2016;44:3346-3358.
36. Malandain M, Maheu N, Moureau V. Optimization of the deflated conjugate gradient algorithm for the solving of elliptic equations on massively parallel machines. *J Comput Phys*. 2013;238:32-47.
37. Liu WK, Jun S, Zhang YF. Reproducing kernel particle methods. *Int J Numer Methods Fluids*. 1995;20:1081-1106.
38. Idel'cik IE. In: Eyrolles, ed. *Memento Des Pertes de Charges*. 3rd ed. EDF; 1986.
39. Ouared R, Larrabide I, Brina O, et al. Computational fluid dynamics analysis of flow reduction induced by flow-diverting stents in intracranial aneurysms: a patient-unspecific hemodynamics change perspective. *J Neurointerv Surg*. 2016;8:1288-1293.
40. Zhang M, Tupin S, Anzai H, et al. Implementation of computer simulation to assess flow diversion treatment outcomes: systematic review and meta-analysis. *J Neurointerv Surg*. 2021;13:164-170.
41. Müller T, Meyer J, Kasper G. Low Reynolds number drag and particle collision efficiency of a cylindrical fiber within a parallel array. *J Aerosol Sci*. 2014;77:50-66.
42. Marheineke N, Wegener R. Modeling and application of a stochastic drag for fibers in turbulent flows. *Int J Multiph Flow*. 2011;37:136-148.

How to cite this article: Bérod A, Mut F, Cebral J, Mendez S, Chnafa C, Nicoud F. Assessing a heterogeneous model for accounting for endovascular devices in hemodynamic simulations of cerebral aneurysms. *Int J Numer Meth Biomed Engng*. 2023;e3762. doi:10.1002/cnm.3762

APPENDIX

EXPRESSION OF THE LINEIC FORCES FOR THE HIM MODEL

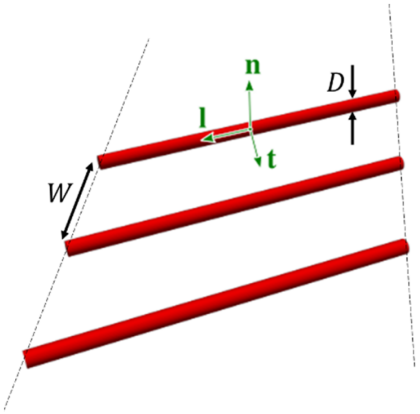

FIGURE A1 Local orthonormal basis used for the computation of the force induced by a family of parallel wires onto the fluid.

As detailed in Reference 22 and quickly recalled in section 2.2.2, the HIM methodology relies on lineic forces applied to each wire segment to represent the momentum loss induced by its presence in the flow. To compute these forces, the device is seen as the superposition of two families of parallel struts and any interactions between the two families are neglected. Then, a local orthonormal basis $(\mathbf{n},\mathbf{l},\mathbf{t})$ is built, where $\mathbf{n}$ is the direction normal to the wires plane, $\mathbf{l}$ is the wire direction and $\mathbf{t}$ belongs to the plane containing the struts. The incident velocity $\mathbf{U}_\infty$ is then decomposed into a normal component $\mathbf{U}_\infty \cdot \mathbf{n}$, a longitudinal component along the wire direction $\mathbf{U}_\infty \cdot \mathbf{l}$ and a tangential component $\mathbf{U}_\infty \cdot \mathbf{t}$. The following correlations are used to assess the force in the same three directions, which depend on the incident velocity and wire characteristics. The interested readers should refer to Berod et al[22] for the most technical details relevant to the practical computation of the forces induced by the network of struts.

NORMAL DIRECTION

The projection of the force along the $\mathbf{n}$ direction reads:

$$\boldsymbol{F_n} = C_D \rho D \frac{(\mathbf{U}_\infty \cdot \mathbf{n})^2}{2}$$

where ρ is the fluid density and D the strut diameter while the drag coefficient C_D depends on the normal Reynolds number R_e^n (based on the wire diameter and normal velocity $\mathbf{U}_\infty \cdot \mathbf{n}$) and the interwire distance to diameter ratio W/D as described in References 22,41.

LONGITUDINAL DIRECTION

The projection of the force along the $\mathbf{l}$ direction reads:

$$\boldsymbol{F_l} = C_l \rho \frac{\nu^2}{D} R_e^n R_e^l$$

where ν is the fluid kinematic viscosity and the drag coefficient C_l depends on the normal Reynolds number as proposed by Marheineke and Wegener.[42] The interwire distance to diameter ratio W/D does not appear since the wire interactions are not accounted for in the longitudinal direction.[22]

TANGENTIAL DIRECTION

The model relies on the drag force for an isolated wire which writes:

$$\boldsymbol{F}_{\boldsymbol{t},\mathbf{0}} = C_{\boldsymbol{t}}\,\rho\frac{\nu^2}{D}R_e^{t\,2}$$

where the drag coefficient C_t depends on the tangential Reynolds number R_e^t as proposed by Marheineke and Wegener.[42] The actual force along the tangential direction is then built from $\boldsymbol{F}_{\boldsymbol{t},\mathbf{0}}$ as

$$\boldsymbol{F}_{\boldsymbol{t}} = G\boldsymbol{F}_{\boldsymbol{t},\mathbf{0}}$$

where the G factor was derived from geometric considerations involving W/D and the angle between $\mathbf{U}_\infty$ and $\mathbf{t}$ to account for the fact that the drag induced by a wire is reduced when it stands in the wake of another wire. See Berod et al[22] for more technical details about the construction of G.